photonics

MDPI

Article

Buffer Gas Pressure Optimization for Atomic Spin Relaxation Suppression in Ultra-High-Sensitivity SERF Magnetometers

Siran Li [1], Xiaotian Lu [1,*], Yinghui Zhang [1], Yafang Zou [1], Yanning Ma [2] and Li Cao [3,*]

[1] Institute of Remote Sensing Satellite, China Academy of Space Technology, Beijing 100094, China
[2] National Key Laboratory of Metrology and Calibration, Beijing Institute of Radio Metrology and Measurement, Beijing 100854, China
[3] Beijing Institute of Space Launch Technology, Beijing 100076, China
* Correspondence: lxt821404732@hotmail.com (X.L.); caoli722@buaa.edu.cn (L.C.)

Abstract

Optically pumped magnetometers (OPM) are core quantum payloads for geomagnetic remote sensing. Among them, the spin-exchange relaxation-free (SERF) OPM with aT-level ultimate sensitivity stands as mainstream. While enlarging the alkali-metal vapor cell of the SERF OPM enhances sensitivity, it triggers complex atomic spin relaxation, notably intensified magnetic field gradient relaxation. To address the dilemma of atomic spin relaxation regulation and the engineering requirements of ultra-high-sensitivity SERF magnetometers, this paper constructs an analytical model of the total relaxation rate that comprehensively considers wall-collision relaxation, spin-destruction collision relaxation, and longitudinal/transverse magnetic field gradient relaxation, etc. The analytical relationship between buffer gas pressure and total relaxation rate for a commonly used spherical vapor cell is derived, revealing the intrinsic correlation among cell size, atomic spin relaxation, and optimal pressure. Based on the theoretical model, the filling parameters of the vapor cell are optimized, and experimental measurements are carried out. The theoretical relaxation results are highly consistent with the experimental ones, realizing the precise optimization of buffer gas pressure. The optimization method proposed in this paper provides a theoretical basis and parameter guidance for the engineering preparation of alkali-metal vapor cells for high-sensitivity SERF magnetometers in remote sensing applications.

Keywords: SERF optically pumped magnetometer; alkali-metal vapor cell; atomic spin relaxation; buffer gas pressure; magnetic field gradient relaxation; geomagnetic remote sensing

1. Introduction

Atomic magnetometers feature high sensitivity, small size, low power consumption, and no hysteresis, and have been widely used in remote sensing fields such as global geomagnetic field modeling [1], airborne magnetic anomaly exploration [2], satellite space magnetic field detection [3–6], and seismic electromagnetic monitoring [7,8]. Among them, the optically pumped magnetometer (OPM) based on the spin-exchange relaxation-free (SERF) regime suppresses spin-exchange relaxation through high-density alkali-metal atoms and an extremely weak magnetic field environment, greatly prolonging the atomic transverse relaxation time [9,10]. Its ultimate sensitivity can thus reach the aT level, far exceeding that of traditional OPMs and fluxgate magnetometers, making it the preferred technical route for next-generation spaceborne and airborne remote sensing magnetic detection [11–13].

Check for updates

Received: 29 April 2026
Revised: 23 May 2026
Accepted: 25 May 2026
Published: 1 June 2026

Copyright: © 2026 by the authors. Licensee MDPI, Basel, Switzerland. This article is an open access article distributed under the terms and conditions of the Creative Commons Attribution (CC BY) license.

The theoretical ultimate sensitivity of a SERF magnetometer is determined by atomic spin projection noise and affected by atomic spin relaxation. Therefore, suppressing atomic spin relaxation is the key to improving the sensitivity. Happer et al. first proposed the theory of the SERF effect and revealed the suppression mechanism of spin-exchange relaxation [11]. Romalis established an alkali-metal atom relaxation model, clarifying that spin-destruction collision, wall-collision, and magnetic field gradient are the main relaxation sources of SERF magnetometers [14]. Zhen et al. analyzed the wall-collision relaxation mechanism of spherical vapor cells and derived the wall relaxation rate formula under diffusion control [15]. Romalis et al. derived the analytical relationship between magnetic field gradient and atomic relaxation rate, confirming that gradient relaxation is proportional to the square of buffer gas pressure [16]. Notably, increasing the volume of the alkali-metal vapor cell of a SERF magnetometer can directly increase the effective measurement volume and reduce spin projection noise [17]. Therefore, to improve the ultimate sensitivity, large-sized alkali-metal vapor cells should be selected as much as possible. However, under the condition of large vapor cells, the internal magnetic field distribution of the cell is uneven, and magnetic field gradient relaxation becomes the main loss term of large-cell SERF magnetometers, and the relaxation mechanism is more complex [18,19].

From the analysis of various relaxation mechanisms, buffer gas is the core medium for regulating atomic relaxation. Filling inert buffer gases such as ^{4}He can suppress the wall-collision relaxation between alkali-metal atoms and the cell wall, but excessive pressure will intensify the spin-destruction collision between alkali-metal atoms and buffer gas. Meanwhile, magnetic field gradient relaxation shows a nonlinear law with the change of buffer gas pressure. Therefore, there is a global optimal value of buffer gas pressure, which can minimize the total relaxation rate and maximize the coherence time [20–22]. Walter et al. established a collision relaxation model between alkali-metal atoms and buffer gas and provided spin-destruction collision cross-section parameters [23]. Burt et al. optimized the buffer gas for micro optically pumped magnetometers and achieved increase in coherence time [24]. Zhai et al. narrowed the magnetic resonance linewidth by optimizing the buffer gas ratio, but ignored the influence of magnetic field gradient relaxation [25]. Most of these studies focus on small-volume vapor cells and ignore the coupling effect of gradient relaxation in large vapor cells.

In summary, existing buffer gas optimization models mostly ignore magnetic field gradient relaxation, are only applicable to small-volume vapor cells, and thus cannot adapt to the working conditions of large-volume SERF vapor cells. There is a lack of an analytical model of total relaxation rate that comprehensively analyzes multiple relaxation mechanisms, including gradient relaxation. The optimal buffer gas pressure relies on experimental trial and error, and there is insufficient research on the quantitative relationship between pressure and relaxation for vapor cells of different sizes. The lack of an accurate basis for engineering cell filling parameters restricts the improvement of magnetic field measurement sensitivity. Therefore, carrying out research on buffer gas pressure optimization coupled with magnetic field gradient relaxation is of important academic value and engineering significance for improving the sensitivity of SERF magnetometers and supporting the engineering application of remote sensing quantum payloads.

In this paper, we (1) systematically analyzes the four constituent mechanisms of atomic spin relaxation in SERF magnetometers, focusing on establishing an analytical model considering longitudinal/transverse magnetic field gradient relaxation in large vapor cells; (2) derives the quantitative relationship between buffer gas pressure and wall-collision relaxation, spin-destruction collision relaxation, and gradient relaxation, and obtains the optimal buffer gas pressure under different cell radii; (3) builds an experimental

platform to complete magnetic field gradient testing and vapor cell preparation, and verifies the effectiveness of the theoretical model through magnetic resonance linewidth measurement. The research results of this paper can directly serve the cell design and batch preparation of high-sensitivity atomic magnetometers for remote sensing, and provide key technical support for spaceborne geomagnetic detection, airborne resource exploration, and other applications.

2. Theoretical Analysis

OPMs realize magnetic field measurement by optically detecting the change of coherent Larmor precession of alkali-metal atom ensembles under the action of a magnetic field [26,27]. Therefore, SERF magnetic field measurement is limited by the uncertainty principle of quantum mechanics, and there is a standard quantum limit in the measurement results. That is, the ultimate sensitivity of an optically pumped atomic magnetometer is mainly limited by atomic shot noise (spin projection noise) [10]:

$$\delta B = \frac{1}{\gamma\sqrt{nT_2Vt}}, \tag{1}$$

where γ is the gyromagnetic ratio of the alkali-metal ensemble, n is the number density of alkali-metal atoms, T_2 is the transverse relaxation time of the atomic ensemble, V is the effective measurement volume, and t is the measurement time. Increasing the effective atomic interaction volume can significantly improve the ultimate sensitivity of SERF magnetic field measurement. Therefore, to pursue the limit of extremely weak magnetic field detection, SERF magnetometers prefer to adopt large-volume alkali-metal vapor cells. For a vapor cell with a selected volume, it is necessary to maximize T_2 as much as possible.

The analysis of atomic spin relaxation in this work is applicable to common atomic vapor cell compositions, such as potassium, rubidium, and cesium. The values of atomic density and temperature must satisfy the operating conditions of the spin-exchange relaxation-free (SERF) regime. To facilitate theoretical derivation and experimental comparison, the constant parameters in the subsequent relaxation model are exemplified by a spherical vapor cell filled with potassium atoms, nitrogen, and helium (^{4}He). Such vapor cell parameters deliver higher theoretical sensitivity. Regarding cell geometry, spherical vapor cells exhibit more uniform gas diffusion and atomic polarization, as well as longer relaxation times, compared to cylindrical or square cells. Regarding cell composition, potassium atoms feature a lower probability of spin-destruction collisions and smaller optical frequency shifts. Helium (^{4}He) has no nuclear spin, thus eliminating additional spin relaxation induced by coupling between nuclear spin and alkali-metal electron spin. Nitrogen (N_2) offers excellent quenching performance at a low cost [26,27].

2.1. Atomic Ensemble Relaxation Process

The relaxation caused by atomic collisions and the interaction of the magnetic field on atoms mainly comes from spin-exchange relaxation, spin-destruction collision relaxation, wall-collision relaxation, and magnetic field gradient relaxation.

2.1.1. Spin-Exchange Relaxation

Spin-exchange relaxation is related to elastic collisions between alkali-metal atoms and the external magnetic field. After the collision of two alkali-metal atoms, the electron spin is exchanged, but the nuclear spin remains unchanged, and the spin-exchange rate is R_{SE}. Therefore, the angular momentum of the atomic spin ensemble is conserved during this collision process, which only leads to the redistribution of atoms among Zeeman

sublevels. However, when the external magnetic field is large, the degenerate Zeeman sublevels split, leading to the Larmor precession of the atomic ensemble, and the total angular momentum corresponds to the opposite Larmor precession, thus causing the relaxation effect. In a weak magnetic field environment, increasing the spin-exchange rate by means of increasing temperature and atomic number density can greatly suppress the relaxation rate, and the atomic ensemble enters the SERF state [11]. Therefore, the influence of spin-exchange relaxation can be ignored when calculating the relaxation of the SERF magnetic field measurement.

2.1.2. Spin-Destruction Collision Relaxation

Spin-destruction collision relaxation is caused by collisions between alkali-metal atoms and themselves or other gas molecules. The angular momentum of the spin ensemble is not conserved during the destruction collision, and atoms redistribute in the ground-state Zeeman sublevels, leading to atomic relaxation. The spin-destruction collision relaxation rate is positively correlated with the collision probability. In SERF magnetic field measurement, spin-destruction collisions mainly include collisions between alkali-metal atoms, collisions between alkali-metal atoms and quenching gas molecules (N_2), buffer gas molecules (^{4}He), etc. The total spin-destruction collision relaxation rate R_{SD} is expressed as [28]:

$$R_{SD} = n_{alkali}\overline{v}_{alkali}\sigma^{SD}_{alkali} + n_{N_2}\overline{v}_{N_2}\sigma^{SD}_{N_2} + n_{He}\overline{v}_{He}\sigma^{SD}_{He}, \quad (2)$$

where n is the number density of alkali-metal atoms or gas molecules; $\overline{v} = \sqrt{8k_BT/\pi M}$ is the relative average velocity of alkali-metal atoms or gas molecules, M is the reduced mass of alkali-metal atoms or gas molecules collisions; σ^{SD} is the spin-destruction collision cross-section. The relevant parameters of potassium atoms are shown in Table 1.

Table 1. Constants Related to Potassium Atom Relaxation Analysis.

Constant	σ^{SD}_K/cm^2	σ^{SD}_{He}/cm^2	$\sigma^{SD}_{N_2}$/cm^2	M_{K-N_2}/g	M_{K-^4He}/g	M_{K-K}/g
Value	1.0×10^{-18}	8.0×10^{-25}	7.9×10^{-23}	27.1×10^{-27}	6.0×10^{-27}	64.86×10^{-27}

2.1.3. Wall-Collision Relaxation

Wall-collision relaxation originates from the interaction between alkali-metal atoms and the cell wall. After the cell wall adsorbs and releases alkali-metal atoms, the released alkali-metal atoms are randomly distributed in the ground-state energy level, leading to the relaxation of the ground-state energy level. Similar to spin-destruction collision relaxation, the wall-collision relaxation rate is also related to the collision probability between alkali-metal atoms and the cell wall. In SERF magnetic field measurement, to suppress wall-collision relaxation, a large amount of buffer gas is filled into the vapor cell. The presence of buffer gas slows down the movement of alkali-metal atoms and reduces their collision probability with the cell wall. Therefore, wall-collision relaxation is related to the diffusion process described by the diffusion equation $\partial P/\partial t = D\nabla^2 P$, where P is the atomic polarizability, and D is the diffusion constant. Using the method of separation of variables to solve the diffusion equation, limited by the boundary condition that the polarizability is always 0 at the cell wall, the wall-collision relaxation rate R_{wall} in a spherical vapor cell can be obtained as [29]:

$$R_{wall} = D_0\left(\frac{(T/273.15\ K)^{3/2}}{p/1\ \text{atm}}\right)\left(\frac{\pi}{r}\right)^2, \quad (3)$$

where $D_0 = 0.35\ \mathrm{cm}^2/\mathrm{s}$ is the diffusion constant of potassium atoms under standard conditions, T is the cell temperature, p is the buffer gas pressure, and r is the radius of the spherical vapor cell.

2.1.4. Magnetic Field Gradient Relaxation

Magnetic field gradient relaxation is caused by the inhomogeneity of the magnetic field sensed by alkali-metal atoms. When no buffer gas is filled, alkali-metal atoms move rapidly in the vapor cell, and the atoms sense the average magnetic field during movement. Since the vapor cell is filled with inert buffer gas (^{4}He), the movement ability of alkali-metal atoms is weakened, and the diffusion distance of alkali-metal atoms becomes smaller. Therefore, atoms can only sense the local magnetic field of the diffusion distance within the coherence time, and the gradient magnetic field sensed by alkali-metal atoms is more obvious. The longitudinal and transverse gradient relaxations can be expressed as [30–32]:

$$R_{gr1} = 2D\frac{\left|\vec{\nabla}B_x\right|^2 + \left|\vec{\nabla}B_y\right|^2}{B_0^2} \times \sum_n \frac{Q(P)}{\left[x_{1n}^2 - 2\right]\left[Q(P) + D^2 x_{ln}^4 B_0^{-2}\gamma^2 r^{-4}\right]}, \tag{4}$$

$$R_{gr2} = \frac{8\gamma^2 R^4\left|\vec{\nabla}B_z\right|^2}{175DQ(P)} + D\frac{\left|\vec{\nabla}B_x\right|^2 + \left|\vec{\nabla}B_y\right|^2}{B_0^2} \times \sum_n \frac{Q(P)}{\left[x_{1n}^2 - 2\right]\left[Q(P) + D^2 x_{ln}^4 B_0^{-2}\gamma^2 r^{-4}\right]}, \tag{5}$$

where B_0 is the static magnetic field sensed by atoms in the vapor cell, $\vec{\nabla}B_x$, $\vec{\nabla}B_y$ and $\vec{\nabla}B_z$ are the triaxial first-order gradient magnetic fields. $Q(P) = \frac{(2I+1)(3+P^2)}{2+2P^2}$ is the slowing-down factor caused by nucleons, which represents the slowdown of the actual precessional angular frequency of alkali metal atoms relative to free electrons and can be regarded as a constant related to the polarizability P and the nuclear quantum number $I = 3/2$ of potassium. x_{ln} is the spatial frequency coefficient, which are the zeros of the derivatives of spherical Bessel functions in order to satisfy the boundary condition of the spin-density matrix as defined and tabulated in [32], where foot script l is the angular momentum and $n = 1,2,\ldots$ labels the solutions in order of increasing magnitude. Our simulation condition in Chapter 3 and 4 retains the value up to $n = 5$ and $l = 1$. This relaxation term is related to the vapor cell pressure, cell size, and triaxial magnetic field gradients. The longitudinal magnetic field gradient ∇B_z affects the transverse relaxation R_{gr2} and is proportional to the square of the magnetic field gradient $|\nabla B_z|^2$; the transverse magnetic field gradients ∇B_x and ∇B_y affect the longitudinal relaxation R_{gr1}, and the gradient relaxation rate is proportional to $\left(|\nabla B_x|^2 + |\nabla B_y|^2\right)$. Both are affected by the static magnetic field in the vapor cell, i.e., remanence.

To obtain the optimal theoretical sensitivity, it is necessary to maximize the spin-polarized transverse relaxation time T_2. Therefore, it is necessary to analyze the atomic spin ensemble relaxation, determine the composition of each relaxation term, and its contribution to T_2:

$$\frac{1}{T_2} = \frac{R_{\mathrm{tot}}}{Q(P)} = \frac{1}{Q(P)}(R_{\mathrm{se}} + R_{\mathrm{sd}} + R_{\mathrm{op}}) + R_{\mathrm{wall}} + R_{gr1} + R_{gr2}, \tag{6}$$

where R_{tot} is the total relaxation rate, defined as the sum of relaxation rates R_{rel} (originating from atomic collisions and magnetic fields) and optical pumping rate (originating from light-atom interaction). In the SERF regime, all relaxation terms are mutually independent and can be linearly superimposed [26]. $R_{\mathrm{op}} = I_{\mathrm{op}}\sigma_{\mathrm{op}}/Ah\nu$ is defined as the optical pumping rate, i.e., the absorption rate of circularly polarized photons. This parameter

can be calculated from the pumping light intensity I_{op}, the optical pumping absorption cross-section σ_{op} of alkali-metal atoms, the spot area A of the pumping beam, Planck's constant h, and the pumping light frequency ν. Under the combined influence of the optical depth and the polarization effect exerted by the pump light on alkali metal atoms, the pumping rate can be derived and solved by the Lambert Function. The coupling of R_{op} with transverse relaxation rates including R_{wall}, R_{SD}, R_{gr2} is negligible [30]. Ultimately, the transverse relaxation time can be quantified via the magnetic resonance linewidth $\Delta\omega$:

$$T_2 = \frac{1}{2\pi\Delta\omega}, \tag{7}$$

2.2. Buffer Gas Pressure

Aiming at the technical difficulty of the improvement on atomic spin relaxation time, the relaxation suppression method is studied based on the analysis of the relaxation composition of the electron spin ensemble. By adjusting the parameters of each component in the alkali-metal vapor cell, the alkali-metal vapor cell parameter design with optimal relaxation is realized. The atomic spin relaxation is suppressed by optimizing the air pressure of the alkali-metal vapor cell, and the ultimate sensitivity index of the magnetometer is improved.

For high-performance alkali-metal vapor cell design, it is first necessary to optimize the parameters of the amount of gas filled into the vapor cell according to the application object and environmental conditions, and then the interior of the alkali-metal vapor cell is filled with high-purity and pollution-free working gases (such as quenching, buffering, and other functions). Diatomic molecules are selected as quenching gas to eliminate the electron capture effect, usually nitrogen, which accounts for a small proportion of 50~100 Torr in the cell. Buffer gas can effectively suppress the relaxation process between alkali-metal atoms and the cell wall, and helium is usually used as the buffer gas component; the content of buffer gas is dozens of times that of quenching gas. Combined with the theoretical analysis of each relaxation term mentioned above, the buffer gas participates in the formation of various relaxations. The higher the buffer gas pressure, the greater the spin-destruction collision relaxation and gradient relaxation, and the smaller the wall-collision relaxation. Since the total relaxation is the sum of multiple relaxations, there is an optimal value of buffer gas pressure p to minimize the total relaxation. The optimal pressure value is related to temperature, cell size, magnetic field gradient, alkali-metal atom type, and other factors. To quantitatively analyze the optimal value of buffer gas pressure, it is necessary to build a SERF magnetometer for theoretical simulation and experiment.

3. Experimental Setup

3.1. OPM Design and Parameter Measurement

The structure of the SERF magnetometer built in this research is shown in Figure 1, and its structural setup is basically consistent with other previous research teams [33]. The vapor cell is spherical, containing potassium (K) alkali metal, nitrogen (N_2) as quenching gas, and helium (^{4}He) as buffer gas. The cell is heated to 200 °C by an oven suspended in the center of the vacuum chamber. Calibrated triaxial coils are wrapped around the vacuum chamber and driven by a function generator (Keysight, 33500B), which can generate static and sinusoidal magnetic fields. Both the vacuum chamber and the coils are wrapped with magnetic shielding. Both the pump and probe laser sources are distributed Bragg reflector (DBR) lasers. The pump beam is expanded to 25 mm and adjusted to circularly polarized light through a polarizer and a quarter-wave plate ($\lambda/4$). The probe light has a detuning to obtain the maximum signal intensity and is expanded to a diameter of 5 mm. The probe light is polarized by a polarizer (Glan-Taylor prism) and modulated by a photoelastic modulator (PEM). A quarter-wave plate is used to change the ellipticity of the light. Finally,

the modulated light is detected by a photodetector (PD), and the photodiode signal is demodulated by a lock-in amplifier 1 (LIA1) (HF2LI, Zurich Instrument). A sinusoidal current generated by the function generator is applied to the coil to generate a triaxial sinusoidal magnetic field. An additional lock-in amplifier 2 (LIA2) is used, whose input is triggered by the function generator. LIA2 outputs the amplitude-frequency response R required for the experiment.

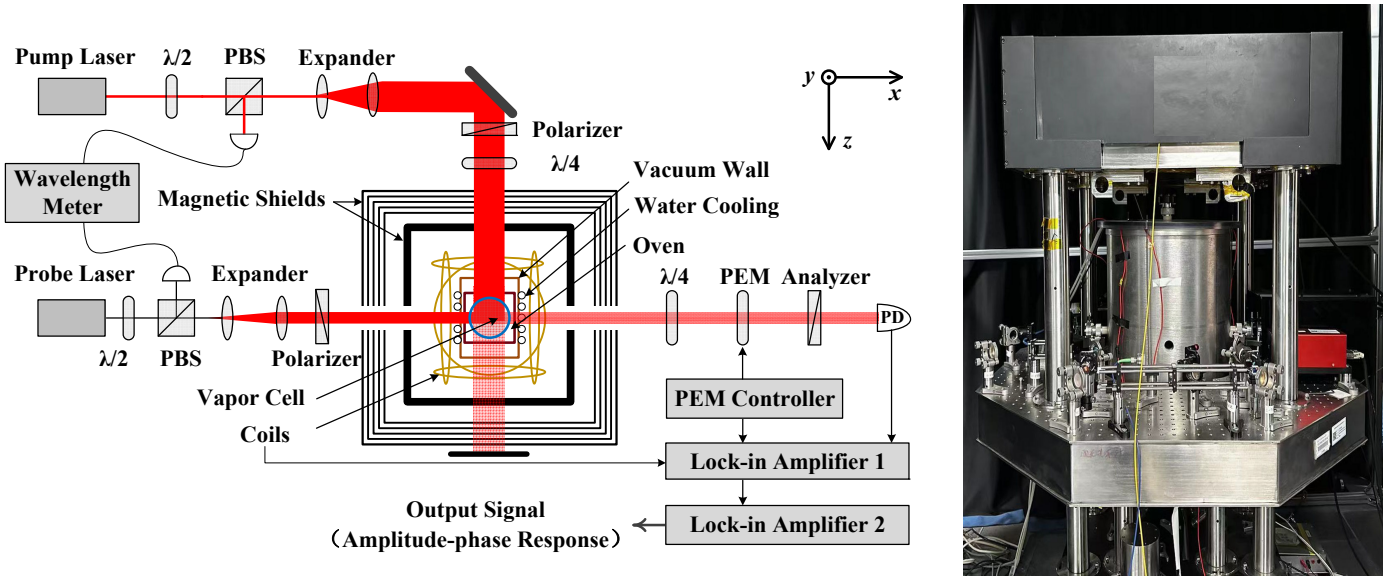


Figure 1. Schematic diagram of the atomic magnetometer structure and the photograph.

3.2. Determination of Vapor Cell Preparation Parameters

The alkali-metal vapor cell is the sensitive core of the ultra-high-sensitivity SERF OPM. Increasing the volume of the atomic vapor cell can increase the effective interaction volume of alkali-metal atoms, reduce the atomic spin projection noise, and effectively improve the theoretical sensitivity limit of the atomic magnetometer, as shown in Equation (1). Therefore, ultra-high-sensitivity atomic magnetometers select the largest possible alkali-metal vapor cells (diameter > 20 mm). Limited by the structure of our magnetometer, the maximum spherical alkali-metal vapor cell that can be used in this research is 25 mm in diameter. However, the relaxation of large-sized alkali-metal vapor cells is greatly affected by the gradient magnetic field. Therefore, it is necessary to test the gradient remanence of the SERF magnetometer to calculate and estimate more accurate vapor cell preparation parameters. Before using the OPM we built, the magnetic shield is first degaussed, and then the remanence gradient test is carried out. The probe of a metrological fluxgate magnetometer (National Institute of Metrology, China, CTW-6 W) is fixed in a long non-magnetic plastic tube marked with scales to test the magnetic field gradient in the magnetic shield. By changing the position of the fluxgate magnetometer, the remanence at different positions is measured, so as to obtain the remanence gradient in the barrel. Considering that the fluxgate magnetometer itself has a magnetic zero-offset error, the probe should be measured once in the forward and reverse directions during measurement, and the magnetic field measurement value, eliminating the zero-offset error, is obtained by dividing the difference between the readings by 2. The test results show that the remanence gradient in the x-direction is 0.45 nT/cm, the remanence gradient in the y-direction is 0.45 nT/cm, and the remanence gradient in the z-direction is 0.47 nT/cm. Based on this condition and Equations (2)–(6), the longitudinal and transverse gradient relaxations of the potassium vapor cell are calculated, and the curves of the optimal buffer gas pressure under different cell radii are shown in Figure 2. The optimal pressure value decreases with the increase

of cell radius, and the influence of gradient relaxation on the optimal buffer gas pressure increases with the increase of cell radius. Restricted by application conditions such as miniaturization requirements and cost control, the cell size cannot be infinitely large, and the optimal pressure varies with cell size. Therefore, based on the theoretical derivation in Chapter 2, we aim to obtain the optimal pressure corresponding to cells of various radii, providing references for cell preparation of different SERF magnetometers. Several typical sizes are summarized in Table 2 according to the results of Figure 2. The optimal buffer gas pressure in Figure 2 is acquired by calculating the partial derivative of Equation (6) with respect to pressure p, and the pressure value corresponding to zero partial derivative $\partial R_{\mathrm{tot}}/\partial p = 0$ is regarded as the optimal buffer gas pressure. Fixed operating parameters of the magnetometer, including magnetic field gradient, slowing factor, and temperature required for the calculation, are listed in Table 3. According to Figure 2, we can determine the preparation parameters for the vapor cells and the finished preparation.

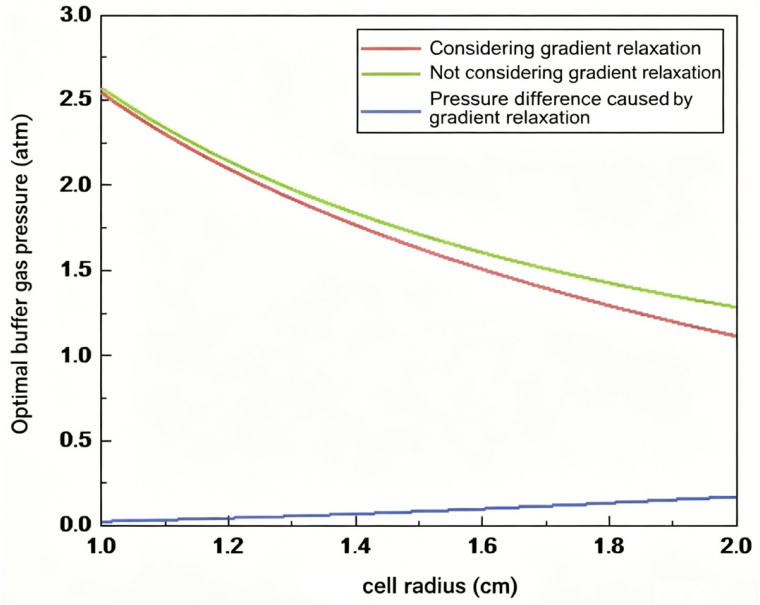


Figure 2. Variation of the optimal buffer gas pressure versus vapor cell radius. atm represents standard atmospheric pressure (1 atm = 101,325 Pa). The *x*-axis denotes the radius of the alkali-metal vapor cell, and the *y*-axis represents the optimal cell pressure obtained by simulation. The red curve corresponds to the optimal buffer gas pressure considering magnetic field gradient relaxation, the green curve indicates the optimal pressure without considering gradient relaxation, and the blue curve shows the pressure difference between the two conditions. The optimal buffer gas pressure in Figure 2 is acquired by calculating the partial derivative of Equation (6) with respect to pressure p, and the pressure value corresponding to zero partial derivative is regarded as the optimal buffer gas pressure.

Table 2. Typical values of buffer gas optimization parameters for vapor cells of different sizes.

Vapor Cell Radius/cm	Optimal ^{4}He Pressure/atm (Without Gradient Relaxation Consideration)	Optimal ^{4}He Pressure/atm (With Gradient Relaxation Consideration)
1.25	2.07	2.01
1.75	1.47	1.36
2.50	1.03	0.80

Table 3. Experimental Parameters.

Item	Parameter
Vapor Cell	Spherical K cell, diameter 25 mm; 50 Torr N2; 2.01 atm ^{4}He
Lasers	Pump: 770.108 nm; Probe: 770.238 nm
Polarization	Steady-state polarizability P ≈ 0.5; slowing-down factor Q(P) = 5.2
Magnetic Shielding	*x*-axis: central remanence of 0.20 nT, gradient remanence of 0.45 nT/cm; *y*-axis: central remanence of 0.25 nT, gradient remanence of 0.45 nT/cm; *z*-axis: central remanence of 0.40 nT, gradient remanence of 0.47 nT/cm.
Coils	*z*-axis: 197.64 nT/mA *x*-axis: 88.93 nT/mA *y*-axis: 88.78 nT/mA
Magnetic Compensation	*x*-axis: 81 pT, *y*-axis: 286 pT, *z*-axis: 553 pT
Electronics	PEM modulation frequency: 50.136 kHz, modulation angle: 0.08 rad LIA: preamplifier gain 10^5, filter bandwidth 200 Hz; sampling frequency: 899 Hz
Heating	200 °C, 100 kHz square wave, ±5 mK

The typical optimal buffer gas pressures for vapor cells of different sizes are listed in Table 2. It can be seen that with the increase of vapor cell size, the influence of gradient relaxation becomes more obvious and cannot be ignored. For a 25 mm diameter positive pressure vapor cell, the optimal buffer gas parameter at 0 °C temperature, considering gradient relaxation, is 2.01 atm (corresponding to a pressure value of about 430 Torr at liquid nitrogen temperature during vapor cell preparation). The alkali-metal vapor cell is thus prepared based on this parameter and installed in the center of the OPM to complete the construction.

4. Results

As analyzed in Chapter 2, the atomic spin ensemble relaxation originates from atomic collisions, the interaction of external light-magnetism on atoms, etc. The relaxation caused by collisions includes spin-exchange relaxation, spin-destruction collision relaxation, and wall-collision relaxation; the relaxation caused by light-atom interaction includes relaxation caused by circularly polarized pump light; the relaxation caused by the magnetic field includes magnetic field gradient relaxation. To obtain the optimal theoretical sensitivity, it is necessary to optimize and test the electron spin ensemble relaxation, determine the composition of each relaxation term in the alkali-metal vapor cell, and the contribution of each relaxation term to the system output, so as to maximize the spin-polarized relaxation time. The premise of measuring the transverse relaxation time is to measure the magnetic resonance linewidth. As shown in Equation (7), the transverse relaxation time is calculated by the magnetic resonance linewidth.

4.1. Simulation

The magnetometer developed in this study is applicable to a 25-mm cell, so a 25-mm cell is fabricated for comparative verification based on the data from Figure 2 and Table 3. Substituting this size into the equations in Chapter 2 helps calculate the bandwidth corresponding to relaxation terms under different pressures. Based on the experimental setup conditions in Table 3 and Equations (2)–(7), a theoretical simulation is carried out on the variation mechanisms of relaxation with buffer gas pressure for a 25 mm diameter vapor cell, as shown in Figure 3. Based on the simulation results of magnetic resonance linewidth, the linewidth of the SERF magnetometer is 3.7 Hz with the optimal buffer gas pressure. The total relaxation rate is about 122 s^{-1}. Among them, the pumping rate at the center of the vapor cell is 60 s^{-1} with a corresponding broadening of 1.8 Hz, and the relaxation rate is 62 s^{-1} with a corresponding broadening of 1.9 Hz.

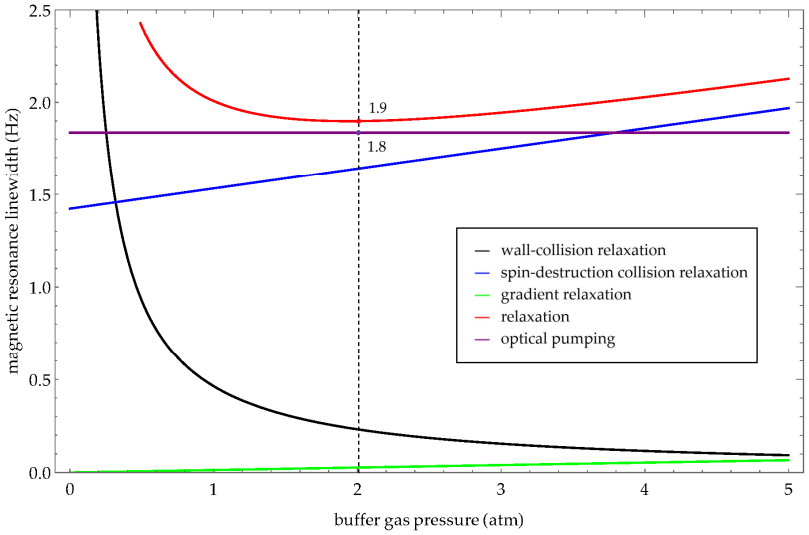


Figure 3. Magnetic resonance linewidth contributions from different relaxation mechanisms as a function of buffer gas pressure. atm represents standard atmospheric pressure (1 atm = 101,325 Pa). The black, blue, and green lines represent the broadening induced by wall-collision relaxation, spin-destruction collision relaxation, and magnetic field gradient relaxation, respectively. The red line shows the total broadening from the sum of the aforementioned relaxation processes. The purple line denotes the broadening induced by optical pumping.

4.2. Measurement

In this research, the magnetic resonance method is used to measure the magnetic resonance linewidth. A sinusoidal excitation magnetic field is applied in the transverse direction of the magnetic field measurement device using a coil. When the frequency of the applied magnetic field is close to the atomic Larmor precession frequency, the magnetic resonance phenomenon will be realized. By sweeping the frequency of the applied magnetic field (0–100 Hz) and lock-in detection of the atomic precession signal, the magnetic resonance curve can be obtained [34,35]. Its frequency response curve conforms to:

$$R(f) = A_0 / \left((f - f_0)^2 + {B_w}^2 \right)^{1/2} + C, \tag{8}$$

where f is the frequency, A_0 is the amplitude coefficient, B_w is the bandwidth, f_0 is the central frequency, and C is the response offset. A DC magnetic field is applied to the sensitive axis of the SERF magnetometer. According to the response amplitude-frequency response curve obtained by the magnetic resonance method, the half-width at half maximum (HWHM) value of the resonance peak is the magnetic resonance linewidth, i.e., the total relaxation rate Rtot/2πQ(P) of the SERF magnetometer. Based on the test results of magnetic resonance linewidth as shown in Figure 4, the system linewidth of the SERF magnetic field measurement device is 4.2 Hz with a coefficient of determination of 0.996, and the total relaxation rate is about 137 s^{-1}. It can be seen from the results that the measured values of magnetic resonance linewidth and relaxation (4.2 Hz, 137 s^{-1}) obtained are equivalent to the simulated values (3.7 Hz, 122 s^{-1}) based on the buffer gas pressure optimization theory in this research, with a consistency of 88%. The difference between the two is mainly due to the filling pressure error caused by the residual gas in the gas pipeline during the vapor cell preparation at liquid nitrogen temperature. In the future, the charging error of the gas chamber preparation will be considered without considering experimental system errors such as laser power fluctuations, residual gradient of magnetic shielding, temperature stability, and detector noise.

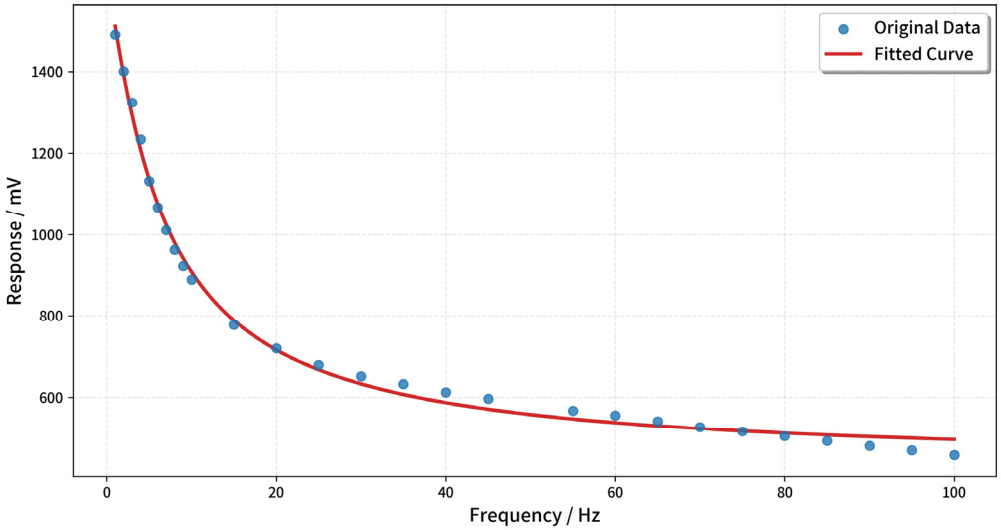


Figure 4. Frequency response test results and fitting curve of SERF magnetometer.

5. Conclusions

Aiming at the technical challenge of atomic spin relaxation regulation and the engineering requirements for alkali-metal vapor cell development, this study systematically analyzes the four major relaxation mechanisms of atomic ensembles, incorporates longitudinal/transverse magnetic field gradient relaxation terms, derives the analytical relationship between buffer gas pressure and total relaxation rate for commonly used spherical potassium vapor cells, and establishes an optimal buffer gas pressure model with the goal of minimizing total relaxation. An experimental platform of a SERF magnetometer with a 25 mm spherical potassium vapor cell as the sensitive core is established, and the optimization of cell filling parameters is completed based on the theoretical model through experimental measurements. The results demonstrate that: when considering gradient relaxation, the optimal ^{4}He buffer gas pressure for the 25 mm vapor cell is 2.01 atm, with a simulated relaxation rate of 122 s^{-1} and a measured relaxation rate of 137 s^{-1}, achieving a high consistency of 88%; the optimal buffer gas pressure decreases monotonically with the increase of vapor cell radius, and gradient relaxation significantly reduces the optimal pressure value. Focusing on the future remote sensing application requirements, this research addresses the technical bottleneck that large-cell SERF magnetometers lack a theoretical basis for buffer gas pressure optimization. The proposed optimization method can provide a theoretical foundation and parameter guidance for the engineering filling preparation of alkali-metal vapor cells, support the improvement of magnetometer sensitivity performance, and is applicable to remote sensing payloads such as spaceborne geomagnetic detection, mineral exploration, and geomagnetic navigation.

Author Contributions: Conceptualization, S.L.; methodology, S.L. and Y.M.; validation, L.C. and Y.M.; investigation, Y.Z. (Yinghui Zhang) and Y.Z. (Yafang Zou); resources, X.L., Y.Z. (Yinghui Zhang) and Y.Z. (Yafang Zou); data curation, S.L. and Y.Z. (Yafang Zou); writing—original draft preparation, S.L.; writing—review and editing, S.L.; supervision, X.L. and L.C.; project administration, X.L. and Y.Z. (Yinghui Zhang); funding acquisition, X.L. All authors have read and agreed to the published version of the manuscript.

Funding: This research was funded by the CASC Young Top-Notch Talent Support Program.

Institutional Review Board Statement: Not applicable.

Informed Consent Statement: Not applicable.

Data Availability Statement: The data related to the paper are available from the corresponding authors upon reasonable request.

Conflicts of Interest: The authors declare no conflicts of interest.

References

1. Friis-Christensen, E.; Lühr, H.; Hulot, G. *Swarm*: A constellation to study the Earth's magnetic field. *Earth Planets Space* **2006**, *58*, 351–358. [CrossRef]
2. Golynsky, A.V.; Golynsky, D.A.; von Frese, R.R. Compiling ship and airborne measurements for the Antarctic's second-generation magnetic anomaly map. *Rus. J. Earth Sci.* **2022**, *22*, 7. [CrossRef]
3. Dikopoltsev, M.; Levy, U.; Katz, O. Magnetic-field-independent spin-exchange relaxation-free magnetometer. *Phys. Rev. A* **2025**, *111*, 032602. [CrossRef]
4. Afach, S.; Buchler, B.C.; Budker, D.; Dailey, C.; Derevianko, A.; Dumont, V.; Figueroa, N.L.; Gerhardt, I.; Grujić, Z.D.; Guo, H.; et al. Search for topological defect dark matter with a global network of optical magnetometers. *Nat. Phys.* **2021**, *17*, 1396–1401. [CrossRef]
5. Bingjun, C.; Bin, Z.; Werner, M.; Roland, L.; Andreas, P.; Michaela, E.; Christian, H.; Irmgard, J. Performance of the engineering model of the CSES high precision magnetometer. In Proceedings of the 2015 IEEE SENSORS, Busan, Republic of Korea, 1–4 November 2015; pp. 1–4. [CrossRef]
6. Budker, D.; Romalis, M.V. Optical magnetometry. *Nat. Phys.* **2007**, *3*, 227–234. [CrossRef]
7. Olsen, N.; Friis-Christensen, E.; Floberghagen, R.; Alken, P.; Beggan, C.D.; Chulliat, A.; Doornbos, E.; Da Encarnação, J.T.; Hamilton, B.; Hulot, G.; et al. The *Swarm* Satellite Constellation Application and Research Facility (SCARF) and *Swarm* data products. *Earth Planets Space* **2013**, *65*, 1189–1200. [CrossRef]
8. Zeren, Z.; Yang, Y.; Yan, R.; Zhang, Z.; Wang, J.; Huang, H.; Xu, S.; Lu, H.; Zhou, N.; Huang, J. The representative scientific results of the China Seismo-Electromagnetic Satellite. *Earthq. Res. Adv.* **2025**, *5*, 100314. [CrossRef]
9. Dang, H.; Maloof, A.; Romalis, M. Ultrahigh sensitivity magnetic field and magnetization measurements with an atomic magnetometer. *Appl. Phys. Lett.* **2010**, *97*, 151110. [CrossRef]
10. Allred, J.; Lyman, R.N.; Kornack, T.W.; Romalis, M.V. High-sensitivity atomic magnetometer unaffected by spin-exchange relaxation. *Phys. Rev. Lett.* **2002**, *89*, 130801. [CrossRef] [PubMed]
11. Happer, W.; Tang, H. Spin-Exchange Shift and Narrowing of Magnetic Resonance Lines in Optically Pumped Alkali Vapors. *Phys. Rev. Lett.* **1973**, *31*, 273–276. [CrossRef]
12. Romalis, M.V.; Dang, H.B. Atomic magnetometers for materials characterization. *Mater. Today* **2011**, *14*, 258–262. [CrossRef]
13. Kitching, J. Chip-scale atomic devices. *Appl. Phys. Rev.* **2018**, *5*, 031302. [CrossRef]
14. Kornack, T.W.; Ghosh, R.K.; Romalis, M.V. Nuclear Spin Gyroscope Based on an Atomic Comagnetometer. *Phys. Rev. Lett.* **2005**, *98*, 230801. [CrossRef]
15. Li, Z.; Zhou, X.; Wu, S.; Zou, S.; Wang, W.; Yin, C. Simulation of wall collision relaxation in alkali metal cells for SERF magnetometer. In Proceedings of the 2023 2nd International Conference on Optical Imaging and Measurement (ICOIM), Xi'an, China, 20–22 October 2023; pp. 242–246. [CrossRef]
16. Savukov, I.M.; Romalis, M.V. NMR detection with an atomic magnetometer. *Phys. Rev. Lett.* **2005**, *94*, 123001. [CrossRef] [PubMed]
17. Kominis, I.K.; Kornack, T.W.; Allred, J.C.; Romalis, M.V. A subfemtotesla multichannel atomic magnetometer. *Nature* **2003**, *422*, 596–599. [CrossRef] [PubMed]
18. Wang, T.; Peng, J.; Li, J.; Liu, Z.; Mao, Y. Suppressing effect of shortening vapor cell stem on polarization-induced magnetic gradient relaxation of Xe in NMR co-magnetometers. *Sens. Actuators A Phys.* **2024**, *374*, 115461. [CrossRef]
19. Liu, Z.; Wang, J.; Diao, W.; He, J.; Wang, J. Optimization of the experimental parameters of cesium CPT system. In *Quantum and Nonlinear Optics II*; SPIE: Bellingham, DC, USA, 2012. [CrossRef]
20. Lu, J.; Zhang, S.; Zhou, Y.; Yan, Y.; Lu, F.; Wang, K.; Zhai, Y.; Ye, M. Optimal buffer gas pressure in dual-beam spin-exchange relaxation-free magnetometers. *Sens. Actuators A Phys.* **2022**, *347*, 113928. [CrossRef]
21. Babb, J.F. Theoretical and experimental studies of line-broadening in alkali metal vapors. In Proceedings of the 22nd International Conference on Photonic, Electronic, Collisions, Santa Fe, NM, USA, 18–24 July 2001; pp. 220–225.
22. Liu, Z.; Diao, W.T.; Wang, J.Y. Investigation of experimental parameters of coherent population trapping with cesium vapor cell. *Acta Phys. Sin.* **2012**, *61*, 233201. [CrossRef]
23. Walter, D.K.; Griffith, W.M.; Happer, W. Magnetic slowing down of spin relaxation due to binary collisions of alkali-metal atoms with buffer-gas atoms. *Phys. Rev. Lett.* **2002**, *88*, 093004. [CrossRef]
24. McWilliam, A.P.; Dyer, S.; Hunter, D.; Mrozowsk, M.; Ingleby, S.J.; Sharp, O.; Burt, D.P.; Griffin, P.F.; McGilligan, J.P.; Riis, E. Optimizing longitudinal spin relaxation in miniaturized optically pumped magnetometers. *Phys. Rev. Appl.* **2024**, *22*, 064024. [CrossRef]

25. Zhai, H.; Li, W.; Jin, G. Improving the Sensitivity of a Dark-Resonance Atomic Magnetometer. *Sensors* **2025**, *25*, 1229. [CrossRef] [PubMed]
26. Budker, D.; Kimball, D. *Optical Magnetometry*; Cambridge University Press: New York, NY, USA, 2013.
27. Auzinsh, M.; Budker, D.; Rochester, S. *Optically Polarized Atoms*; Oxford University Press: New York, NY, USA, 2010.
28. Seltzer, S.J. Developments in Alkali-Metal Atomic Magnetometry. Ph.D. Thesis, Princeton University, Princeton, NJ, USA, 2008.
29. Ito, Y.; Sato, D.; Kamada, K.; Kobayashi, T. Optimal densities of alkali metal atoms in an optically pumped K-Rb hybrid atomic magnetometer considering the spatial distribution of spin polarization. *Opt. Express* **2016**, *24*, 15391–15402. [CrossRef]
30. Fang, X.; Wei, K.; Zhai, Y.; Zhao, T.; Chen, X.; Zhou, M.; Liu, Y.; Ma, D.; Xiao, Z. Analysis of magnetic field gradient effects on atomic spin polarization and relaxation in optically pumped atomic magnetometers. *Opt. Express* **2022**, *30*, 3926–3940. [CrossRef]
31. Cates, G.D.; Schaefer, S.R.; Happer, W. Relaxation of spins due to field inhomogeneities in gaseous samples at low magnetic field and low pressures. *Phys. Rev. A* **1988**, *37*, 2877–2885. [CrossRef]
32. Hasson, K.C.; Cates, G.D.; Lerman, K.; Bogorad, P.; Happer, W. Spin relaxation due to magnetic-field inhomogeneities: Quartic dependence and diffusion-constant measurements. *Phys. Rev. A* **1990**, *41*, 3672–3688. [CrossRef] [PubMed]
33. Xing, B.; Li, S.; Fang, X.; Lu, H.; Ma, D. Effect of optical nonorthogonality on dynamic response in dual-beam atomic magnetometer. *IEEE Trans. Instrum. Meas.* **2025**, *74*, 7000510. [CrossRef]
34. Dusad, R.; Kirschner, F.K.; Hoke, J.C.; Roberts, B.R.; Eyal, A.; Flicker, F.; Luke, G.M.; Blundell, S.J.; Davis, J.S. Magnetic monopole noise. *Nature* **2019**, *571*, 234–239. [CrossRef]
35. Acosta, V.; Ledbetter, M.P.; Rochester, S.M.; Budker, D.; Jackson Kimball, D.F.; Hovde, D.C.; Gawlik, W.; Pustelny, S.; Zachorowski, J.; Yashchuk, V.V. Nonlinear magneto-optical rotation with frequency-modulated light in the geophysical field range. *Phys. Rev. A* **2006**, *73*, 053404. [CrossRef]

Disclaimer/Publisher's Note: The statements, opinions and data contained in all publications are solely those of the individual author(s) and contributor(s) and not of MDPI and/or the editor(s). MDPI and/or the editor(s) disclaim responsibility for any injury to people or property resulting from any ideas, methods, instructions or products referred to in the content.